ICAS 2016
30th Congress of the International Council of the Aeronautical Sciences
DCC, Daejeon, Korea ; September 25-30, 2016

EFFECTS OF SOME NUMERICAL FORMULATION ASPECTS IN HIGH-LIFT CONFIGURATION SIMULATIONS

Enda D.V. Bigarella , Pedro A.G. Ciloni , Leonardo C. Scalabrin
Embraer S.A., São José dos Campos, SP, Brazil

Keywords: *CFD, High-Lift Configurations, Numerical Modelling*

Abstract

High-lift configuration aerodynamics are evaluated through different theoretical and numerical setups with CFD++ tool. Meshes are constructed with $y+ \approx 1$ for typical configurations, in order to represent daily-production engineering applications. Aspects such as preconditioning, turbulence modelling, and cell-reconstruction polynomials are compared in terms of aerodynamic coefficient prediction and simulation convergence. A best-practice setup is achieved with successful prediction of wind-tunnel reference results.

1 Introduction

High-lift devices are fundamental to aircraft take-off and landing performance [1], requiring large efforts in the design of these components, either by CFD simulation or by wind-tunnel testing. High-lift configurations involve all levels of theoretical and numerical formulation complexities in CFD simulations [2, 1, 3].

High-lift configurations are geometrically complex (see Fig. 1), with multiple trailing edges, coves, and surfaces close to each other. The flow presents fluid dynamic features far from the wall such as vortices and wakes, and other aspects which render mesh generation a science in itself [4]. The resulting mesh is generally very refined near the wall, with largely stretched elements, and at certain volume regions to represent flow features away from the wall. The geometry complexity leads to meshes generated under daily-production guidelines with skewed elements and relatively rapid size variation between neighbouring cells. These aspects pose numerical difficulties for spatial and temporal discretisation and convergence [5, 6].

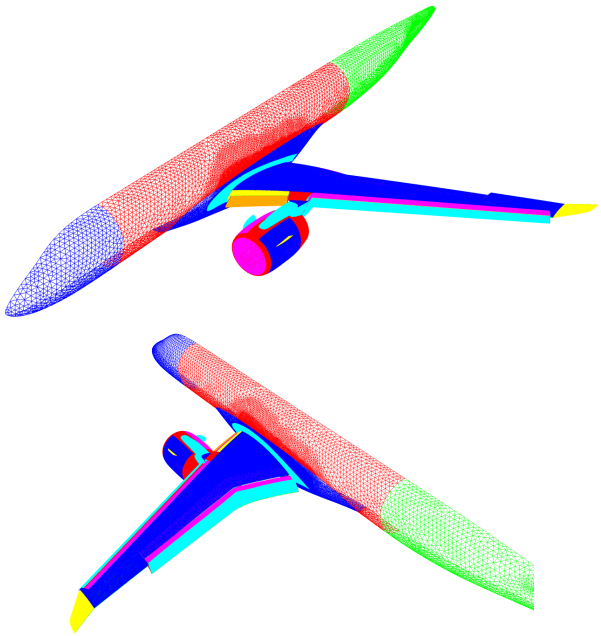

Fig. 1 Overview of a typical high-lift configuration, with slats, flaps, and nacelle chines.

Furthermore, a broad spectrum of velocity distribution in the domain is found. The incoming flow is usually low subsonic. There are large regions with much lower speed flow in wakes and boundary layers, and near-supersonic pockets in leading edge regions, as shown in Fig. 2. Such flow topology also poses difficulties for spatial and temporal integration in terms of numerical stiffness and robustness [7, 8, 9].

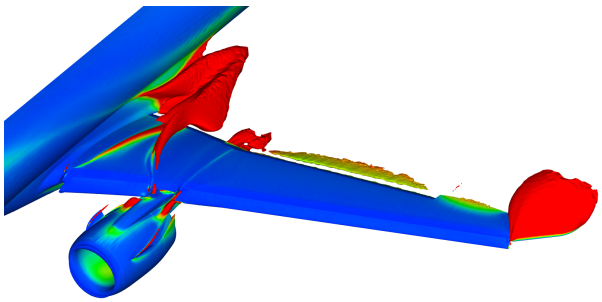

(a) M < 0.1

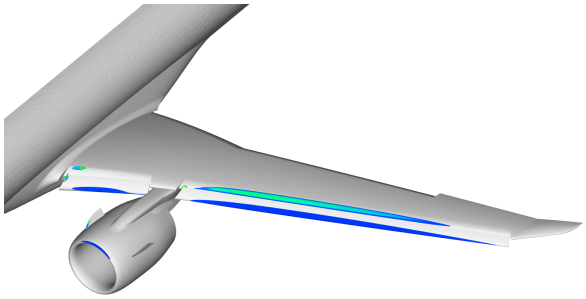

(b) M > 0.5

Fig. 2 Iso-surfaces of Mach number, coloured by the turbulent eddy viscosity, showing low- and high-Mach number regions. For this case, maximum Mach number achieves 0.95 for a freestream Mach number of 0.20.

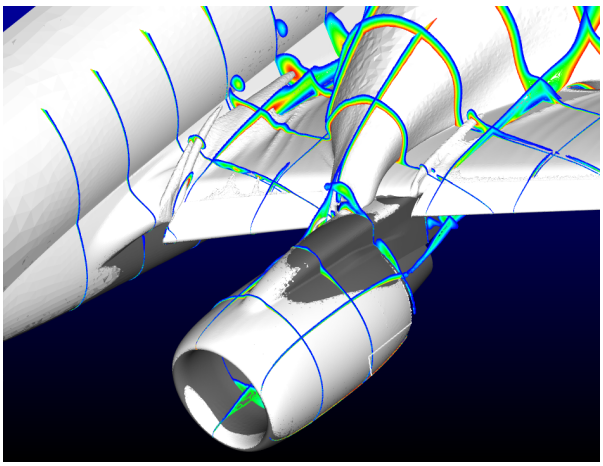

(a) Without chines.

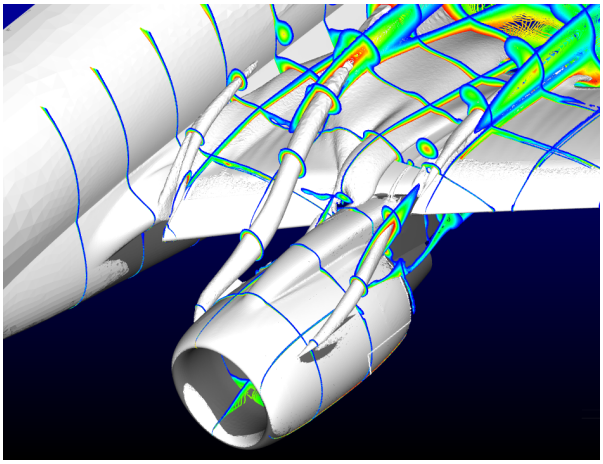

(b) With chines.

Fig. 3 Iso-surfaces of flow total pressure showing slat tip vortices, pylon-wing junction wake, wing-fuselage interaction, nacelle chine vortices and slat wakes. Plots are done at 1 deg. lower than that of the stall with chines installed.

Apart from these aspects, boundary layers, developing wakes, boundary-layer and wake interactions, separation pockets, slat and nacelle chine vortices, as observed in Fig. 3, require adequate turbulence modelling capability, at least under an *ad-hoc* engineering point of view [10, 11, 12]. These flow aspects are more complex than what can be successfully modelled under the Boussinesq hypothesis [13, 10], hence requiring more advanced turbulence models for a better qualitative high-lift flow simulation.

This paper addresses some spatial, temporal and numerical-formulation aspects of high-lift flow simulations, for a mesh generated with daily-production, industry best-practice setup, and turbulence modelling setup suitable for high-lift simulations. The effects of preconditioning, initial conditions, turbulence modelling, and cell polynomial computation are addressed. The commercial CFD++ tool [6] in its version 14.1 is used in the present work, but the conclusions can be extended to other similar CFD codes.

2 Theoretical and Numerical Formulation

2.1 General Aspects

The chosen CFD++ setup solves the density-based, compressible, Reynolds-averaged Navier-Stokes (RANS) equations in conservative form [6]. A finite-volume method (FVM) is employed for any combination of cell elements such as tetrahedra, prisms, wedges and hexahedra. Flux computation at cell faces is performed with the

HLLC [14] scheme. Time integration is performed by a SGS-type, implicit scheme augmented by a W-cycle algebraic multigrid preconditioner [15]. Robustness is further enhanced by residual smoothing, and CFL smoothing is applied in regions where rapid cell size variation is observed. A perfect gas is assumed in the simulations as representative of typical atmospheric commercial flights.

Lift and drag forces are monitored during the iterations as well as a weighted-average of conserved-variable residues, even though actual convergence is hardly achieved for such complex simulations on daily-production meshes. Simulations are performed in a Linux cluster with MPI parallel protocols. A python script is used to create, setup and submit the sequence of various angles of attack (AOA), including the management of previous AOA data as restart for the consecutive AOA.

2.2 Preconditioning

As already indicated, high-lift aerodynamics involve a broad range of velocities, from the very low subsonic to high transonic, or even low supersonic pockets. In special, the very low subsonic regions are of importance in terms of numerical aspects when a density-based, compressible solver is considered [9]. The issues discussed in what follows are related to the inviscid eigenvalues [8] of the equations when weighted by the convective eigenvalue u, written as $\left[1+\frac{1}{M},1,1,1,1-\frac{1}{M}\right]$, where M is the Mach number.

Very low Mach number regions impose a large disparity of these eigenvalues, since when the Mach number $M \to 0$, the acoustic eigenvalues tend to $\pm\infty$. This behaviour is characteristic of a numerically stiff system, which is slow to converge. A preconditioner typically changes the system speed of sound to decrease the eigenvalue disparity to the order of 10 [9], which results in a less stiff numerical system. This modification alters the *intermediate* physical solution since a preconditioner matrix modifies the physically-meaning residue [15]. This aspect is not important for *steady-state* RANS simulations as the preconditioning matrix is ineffective when the residue goes to zero. However, in a typical engineering application, residue convergence to zero is hardly achievable or just not practical, and the effect of the preconditioning in the result of engineering-grade simulations must be verified.

Another very important aspect of preconditioning is its effect in the dissipative behaviour of the flux scheme. Dissipation is an inherent stabilisation feature of numerical schemes [5]. Typically, approximate-Riemann solver schemes such as the HLLC inherently add dissipation proportionally to the system eigenvalues [16]. The dissipative behaviour is dictated by the weighted eigenvalues similarly to the numerical stiffness as previously discussed [8]. Hence, for very low Mach numbers, dissipation terms will scale up rapidly, destroying the steady-state physical behaviour of the conserved properties [7, 8], especially the density, which varies by small proportions in small Mach number regions. Preconditioning the system eigenvalues will avoid the scaling up of the dissipation terms, allowing for a more physically meaning solution.

2.3 Reconstruction Polynomials

The computation of high-order solutions with a finite-volume method requires some sort of property reconstruction in the cell faces for the flux computation [17, 18]. This operation resembles a piecewise-linear property distribution within a cell, denominated "base polynomial" in CFD++ [6]. The property *gradient* in the cell is typically used in FVMs to achieve second-order schemes [18].

The gradient computation for non-uniform, variable element-type, complex meshes is a subject of research yet. One typical and simple method is the use of the Green-Gauss theorem to compute the i-th cell gradient by simply taking the property at every face f that composes the i-th cell

$$\nabla\phi_i = \frac{1}{V_i}\sum_f \bar{\phi}_f \vec{S}_f$$

where V_i is the cell volume, and $\bar{\phi}_f$ is the value of

property ϕ at the cell f face centroid.

For a *centroidal*, or cell-based scheme, the property in the face is usually an average of the centroid property value at the two face-neighbouring elements

$$\bar{\phi}_f = \frac{1}{2}(\phi_i + \phi_{nb})$$

where *nb* is the neighbour of the cell i through face f. For a typical *nodal*, or node-based scheme [19], the property in the face is an average of the properties in its N composing vertices

$$\bar{\phi}_f = \frac{1}{N}\sum_n \hat{\phi}_n$$

and the property at each vertex $\hat{\phi}_n$ is a volume-weighted average of the property at all cells that share that common vertex n. In CFD++, the nodal polynomial is based on computing the gradients at the nodes directly and weighted averaging to the cell centroid, with a few other adaptations and improvements for non-oscillatory behaviour on multi-type element meshes [6, 20].

Reconstruction schemes can lead to local extrema. The classical approach in FVMs is to adopt a limitation on the reconstruction procedure based on oscillation sensors [18]. An enhanced minmod limiter with factor two [6] is used.

2.4 Turbulence Modelling

Flows over high-lift configurations involve highly-3D boundary layer and wake developments, boundary-layer and wake interactions, large separation pockets, slat and nacelle chine vortices, and a mix of these in the same flow field [12]. The Boussinesq hypothesis [13], classically used as the basis for typical engineering turbulence models, is known to fail under such flow conditions [10, 11]. The high-lift application requires going beyond the linear, Boussinesq-based Reynolds-stresses, defined as

$$\tau_{ij} = 2\mu_t\left(S_{ij} - \frac{1}{3}\frac{\partial u_k}{\partial x_k}\delta_{ij}\right) - \frac{2}{3}\rho k\,\delta_{ij}$$

where $S_{ij} = \frac{1}{2}\left(\frac{\partial u_i}{\partial x_j} + \frac{\partial u_j}{\partial x_i}\right)$. *Non-linear* turbulence models [21, 22, 23], with their improved Reynolds-stress prediction seems advantageous and with a wider range of turbulent flow representation, at least qualitatively [12]. These models are based on quadratic or even cubic expansions of the Reynolds-stresses to account for complex flow phenomena, such as multi-dimensional boundary layer and wake development, streamline curvature and separation. In this case, the Reynolds-stresses are written as

$$\tau_{ij} = 2\mu_t\left(S_{ij} - \frac{1}{3}\frac{\partial u_k}{\partial x_k}\delta_{ij}\right) - \frac{2}{3}\rho k\,\delta_{ij} + \rho k\tilde{a}_{ij}$$

where $\tilde{a}_{ij}$ is the anisotropy tensor, which can assume various forms, for instance [21, 22, 23].

Even though a non-linear expansion includes more physics than its linear counterpart, flow field rotation, present in vortex dominated flows, is still not adequately captured. In high-lift applications, slat tip and nacelle-chine vortices strongly induce flow rotation. Classical Boussinesq hypothesis significantly overpredict turbulence production in regions of flow-field rotation, leading to excessively high eddy viscosity levels in the vortex core, eventually smearing it out prematurely [12]. A curvature correction can be added to the turbulence model production to account for this effect [24, 22]. Roughly speaking, the curvature correction leaves the production term unchanged where the strain rate is larger than the vorticity, and decreases the turbulent production where vorticity dominates.

In the current paper, only the Spalart-Allmaras (SA) turbulence model [25] is considered. Based on other studies [2] and confirmed internally, the SA seems to be closer to successful prediction of the aerodynamics of high-lift applications, even without the above-mentioned enhancements. We address here the effect of the two discussed modifications, namely a non-linear constitutive relationship [23] and a curvature correction [24], in the results of the baseline SA model. This model is termed SA-QCR-CC in the current work.

3 Mesh Configurations

The meshes used in the current work are hybrid unstructured meshes with a mix of tetrahedra, prisms, and a few pyramids in the intersection between the prism layer and the tetrahedra. The tetrahedra are generated with a Delaunay algorithm with about 15% spatial growth. Constant-refinement boxes are strategically placed to better capture the nacelle chine vortices and the pylon-wing interaction. Prism layers are constructed to guarantee $y+ \approx 1$ near the wall, and a smooth exponential growth around 13% is usually chosen to guarantee an adequate representation of the boundary layer without largely increasing the mesh size. These aspects are shown in Figs. 4 and 5.

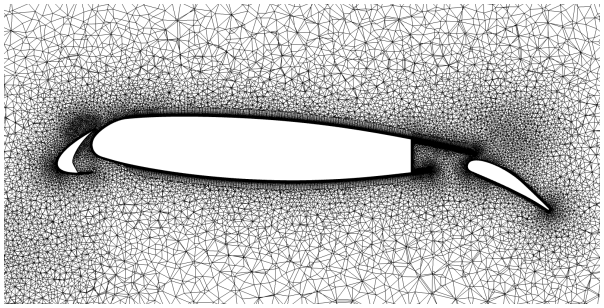

(a) Wing section cove and prism layers.

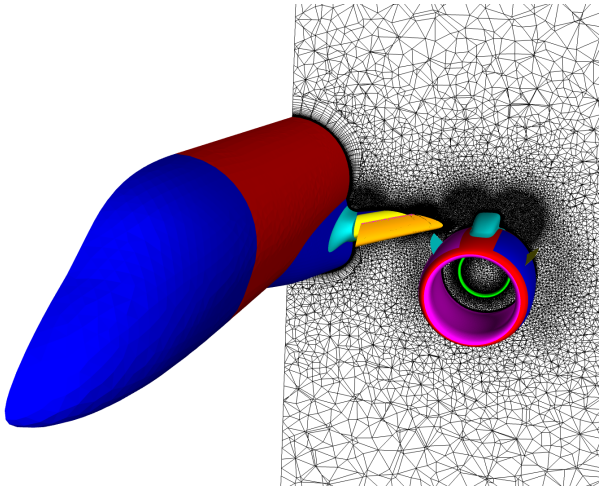

(b) Longitudinal plane across chine-vortex volume refinement.

Fig. 4 Cut planes in a typical low-mounted wing high-lift configuration showing mesh details.

In cove regions, where opposing-wall prism layers may collapse, prism height is decreased to avoid bad elements, as observed in Fig. 4(a). In general meshes have about 110 to 150 million cells and are not hand treated after the automated mesh generation scripts are executed. Hence, they are representative of daily-production, industry best-practice setup. Meshes are generated by either TGrid or ICEM-CFD mesh generation packages.

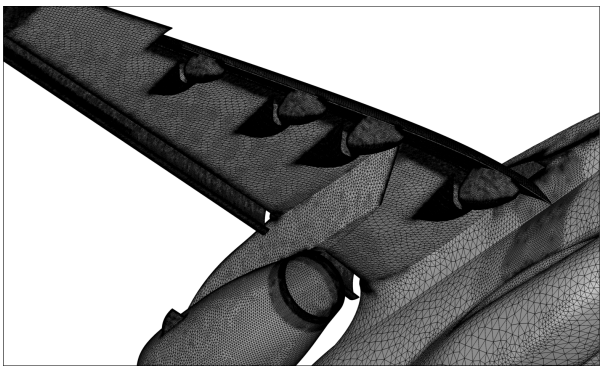

(a) Lower surface wing overview.

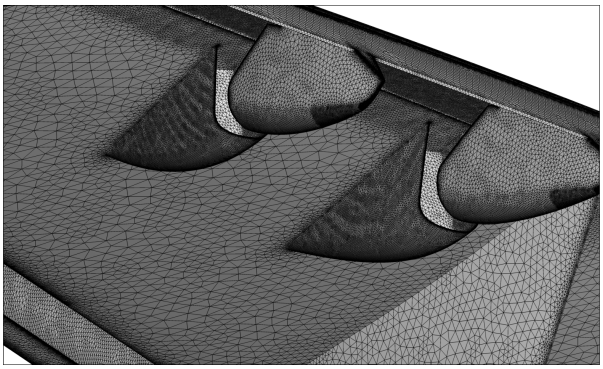

(b) Flap-track fairing detail.

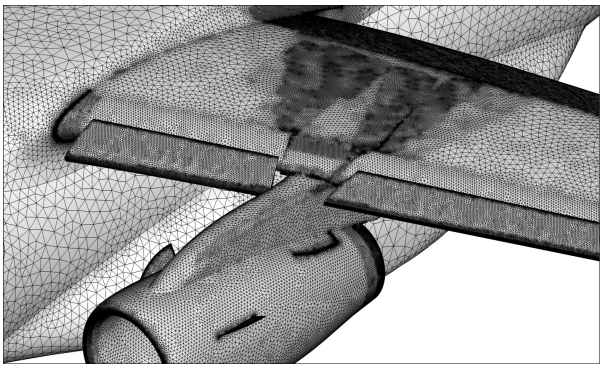

(c) Upper surface wing overview.

Fig. 5 Cut planes in a typical high-mounted wing high-lift configuration showing mesh details.

4 Results and Discussion

In this section the effects of preconditioning, reconstruction polynomials, turbulence model enhancements and using the result from previous AOA as initial conditions are presented and discussed. The analyses are performed mainly in terms of lift curves, but drag, pitching moment and flow topology are also addressed. Low- and high-mounted wing geometries are considered, both at their maximum flap and slat deflections. Meshes are constructed for the wind tunnel geometry, with through-flow nacelles, and simulations are performed at wind tunnel reference conditions, namely, Mach number $M_\infty = 0.2$ and Reynolds number $Re = 3$ million based on the cruise mean aerodynamic chord.

4.1 Preconditioning and Number of Iterations

The effect of solving high-lift problems with compressible or preconditioned formulations is firstly studied. For these simulations, the SA-QCR-CC turbulence model and the centroid-based polynomials are used. Besides the formulation effect, restarting from previous AOA (termed *restart* in the following discussions to simplify the nomenclature) and the number of iterations are also assessed. Figure 6 shows lift curves obtained experimentally and numerically for the low-mounted wing geometry (Fig. 1). Numerical results are obtained for a simpler geometry than that of the wind tunnel, namely, without the flap-track fairings and the slat brackets. This fact partially explains the shift in C_L between numerical and experimental results. The preconditioner with restart option presents a fairly representative result, given the differences in geometry, whereas starting each AOA from scratch results in an earlier stall. The compressible formulation with restart is further off from the experimental results, presenting a lower CL-α slope.

Flows shown in Fig. 3 are obtained for the preconditioned with restart setup for the present geometry. Other aerodynamic data, namely, the drag and the pitching moment coefficients, are also shown in Fig. 7. Similar conclusions about the numerical methodology found in Fig. 6, are also found in Fig. 7, that is, the setup with preconditioning and restart is more representative of the wind tunnel reference data.

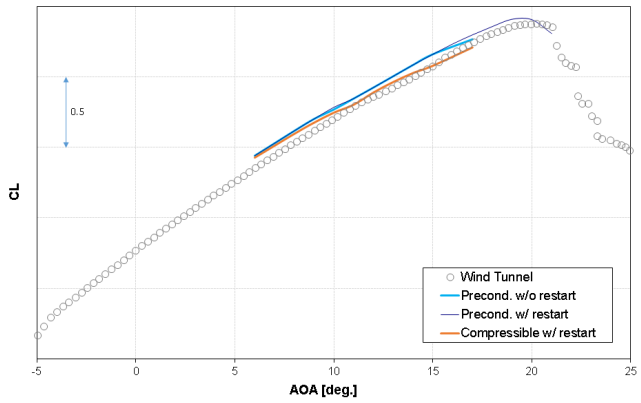

Fig. 6 Lift curves obtained experimentally and numerically, showing the effect of preconditioning and of restarting from previous AOA.

It should be remarked here that the plotted C_L values are obtained as an average of the last 200 iterations for each AOA. The results in Fig. 6 are obtained running 8k iterations per AOA, which guarantees for this configuration a 0.05% stabilisation of the lift for each AOA. The effect of less iterations is shown in Fig. 8 comparing the results for 2k iterations as well. These results are generated with restart from previous AOA along with SA-QCR-CC and centroidal base polynomial. No difference in the lift curve is observed when using preconditioning, whereas solving in compressible mode is quite sensitive to the number of iterations. It should be noted that the result for *less* iterations is misleadingly closer to the experiment for the compressible result.

One interesting aspect of this behaviour is near the build-up of nonlinearities, such as at AOA 10 deg., where the simulation predicts a wingtip separation (observed at 12 to 13 deg. in the wind tunnel). Figure 9 shows the convergence of AOA 10 and 11 deg. for the preconditioned and the compressible setups. The compressible setup was run for 12k iterations for this analysis. It is interesting to observe that the compressible

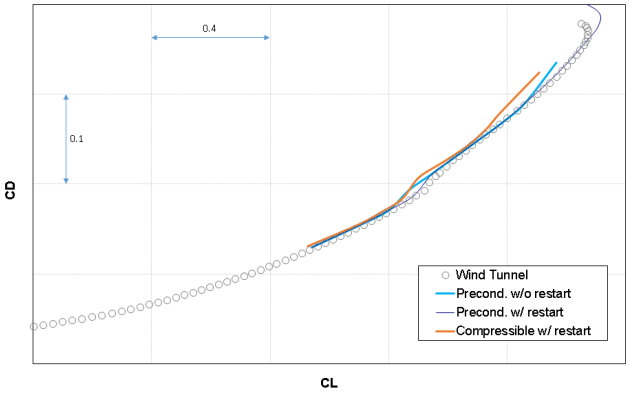

(a) Drag polar.

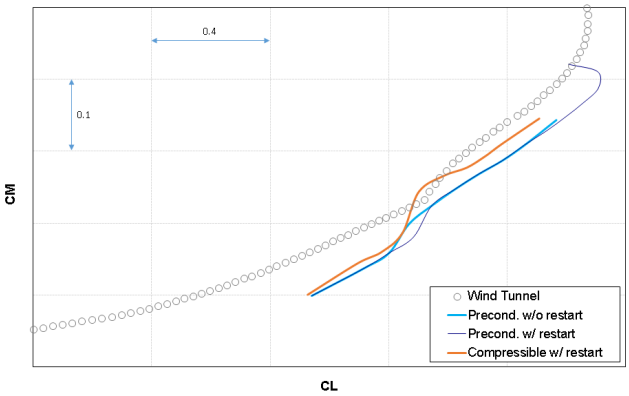

(b) Pitching moment polar.

Fig. 7 Aerodynamic curves obtained experimentally and numerically, showing the effect of preconditioning for low speeds and restarting from previous AOA.

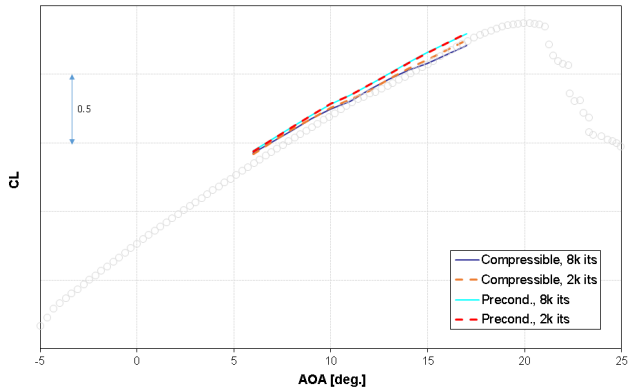

Fig. 8 Lift curves obtained experimentally and numerically, showing the effect of the number of iterations.

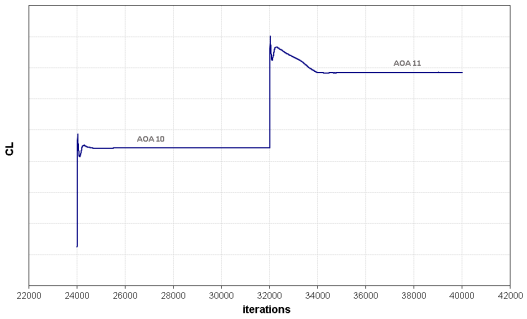

(a) Preconditioned.

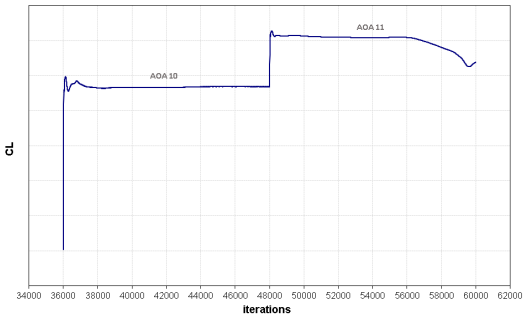

(b) Compressible.

Fig. 9 Lift histories for two angles of attack where the wingtip separates.

run takes longer to sense the wingtip separation, with an exaggerated lift loss effect.

4.2 Reconstruction Scheme

A high-wing geometry, as shown in Fig. 5, is chosen for these analyses. In this case, the flap-track fairings are present in the mesh, but not the slat brackets. An overview of the flow topology is shown in Fig. 10, with pressure coefficient contours over the surface and shearlines. Figure 11 shows lift curves comparing the effect of the reconstruction polynomial. For these simulations, the SA-QCR-CC turbulence model and restart are used. In the current configuration, the node-based reconstruction predicts the stall earlier than the cell-based reconstruction and wind tunnel data. The cell-based reconstruction results are a better representation of the experimental data. This is an interesting aspect to be tested on other numerical solvers which include node-based gradient-computation options to have an

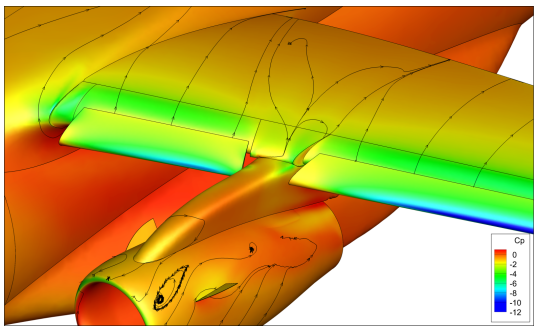

Fig. 10 Flow topology over the high-mounted wing geometry near the stall, with pressure coefficient contours and shearlines.

insight of possible numerical causes for the observed behaviour.

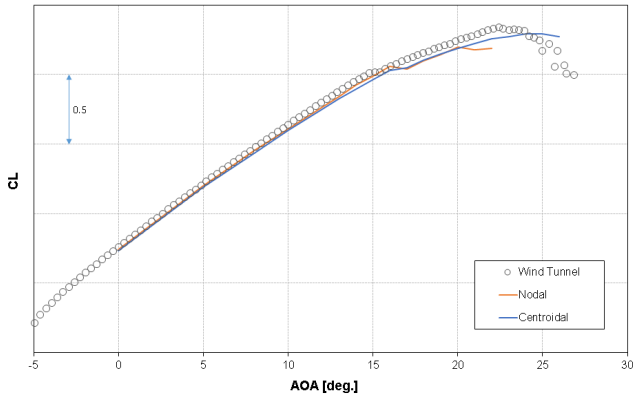

Fig. 11 Lift curves obtained experimentally and numerically, showing the effect of the reconstruction scheme.

4.3 Turbulence Model Enhancements

The effects of the turbulence model enhancements are studied for the flap configuration of Fig. 1. Figure 12 shows the lift curves obtained experimentally and numerically for this case. The simulations are performed using preconditioning with restart. It can be observed in Fig. 12 that the turbulence model modifications considerably affect the maximum lift and the lift curve behaviour. The complete setup with the QCR and CC enhancements presents a better representation of the maximum angle of attack and

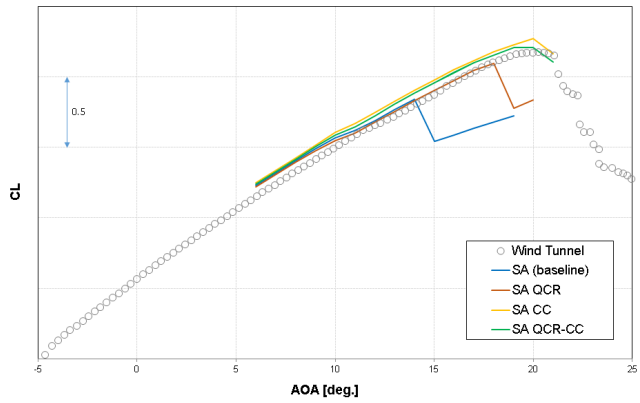

Fig. 12 Lift curves obtained experimentally and numerically showing the effect of the SA turbulence model enhancements.

maximum lift.

This result is a somewhat extreme behaviour specifically found for this geometry, probably due to a strong interaction of the wing with the wake of a relatively large engine. Flow topology at AOA 15 deg. is shown in Fig. 13 for all turbulence model setups of Fig. 12. It can be

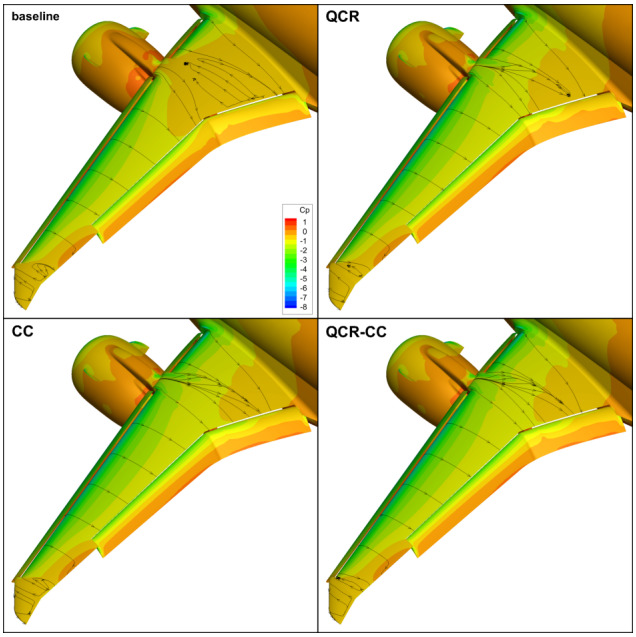

Fig. 13 Pressure coefficient and shearlines for AOA 15 deg. showing the effect of the SA turbulence model enhancements, from the results of Fig. 12.

observed that the difference between the models are mainly found in the pylon-wing intersection region. This region is marked by strong flow three-dimensionality, low dynamic-pressure pockets and wakes. It is undoubtedly a demanding region for the turbulence model. The additional turbulence physics coming from the QCR and CC schemes aid at predicting a better flow topology, avoiding at different levels of compliance an early burst of the pylon-wing junction vortex.

5 Concluding Remarks

An overview of numerical methodology options aimed at enhancing the prediction of aerodynamic data for high-lift configurations is presented. The effect of preconditioning over a compressible RANS formulation is studied along centroidal- and nodal-based gradient computation options. Preconditioning is fundamental for better numerical representation of the aerodynamics of the high-lift configuration due to the extensive very low-Mach number regions in the flow field. This finding is expected but may be a generally underestimated behaviour. The effect of the gradient computation option is not negligible either. This aspect, however, depends on the nodal-based scheme implementation in CFD++, which is not fully available in the literature. Any tentative explanation for this finding with the information currently available would be speculative.

The effects of better modelling the turbulence physics in the Spalart-Allmaras turbulence model, at least qualitatively with the quadratic constitutive relationship and the curvature correction, are measurable. Better representation of the reference wind tunnel data is observed with these options. In general, all the proposed improvements result in closer prediction of the maximum lift at a more representative angle of attack. The use of preconditioning adds the advantage of better convergence for less iterations. This is particularly advantageous when restarting the current angle of attack with data from the previous angle of attack to obtain the entire lift curve. Finally, using the restart significantly improves the results.

References

[1] van Dam, C., "The Aerodynamic Design of Multi-Element High-Lift Systems for Transport Airplanes," *Progress in Aerospace Sciences*, Vol. 38, No. 2, 2002, pp. 101–114.

[2] Rumsey, C. L. and Slotnick, J. P., "Overview and Summary of the Second AIAA High Lift Prediction Workshop," *Journal of Aircraft*, Vol. 52, No. 4, 2015, pp. 1006–1025.

[3] Antunes, A. P., da Silva, R. G., and Azevedo, J. L. F., "On the Effects of Turbulence Modeling and Grid Refinement on High-Lift Configuration Aerodynamic Simulations," *Proceedings of the 28th Congress of the International Council of the Aeronautical Sciences – ICAS 2012*, Paper No. 2012-2.3.1, Brisbane, Australia, Sept. 2012.

[4] Murayama, M., Yamamoto, K., and Kobayashi, K., "Validation of Computations Around High-Lift Configurations by Structured- and Unstructured-Mesh," *Journal of Aircraft*, Vol. 43, No. 2, 2006, pp. 395–406.

[5] Hirsch, C., *Numerical Computation of Internal and External Flows. 2. Computational Methods for Inviscid and Viscous Flows*, chap. 21, Wiley, Chichester, 1991.

[6] Peroomian, O. and Chakravarthy, S., "A 'Grid-Transparent' Methodology for CFD," *35th AIAA Aerospace Sciences Meeting and Exhibit*, AIAA Paper No. 97-0724, Reno, NV, Jan. 1997.

[7] Moura, R. C., Antunes, A. P., Basso, E., Bigarella, E. D. V., and Azevedo, J. L. F., "A Closer Look at Low-Speed Preconditioning Techniques for the Euler Equations of Gas Dynamics," *10th World Congress on Computational Mechanics*, São Paulo, Brazil, July 2012.

[8] Turkel, E., "Preconditioning methods for solving the incompressible and low speed compressible equations," *Journal of Computational Physics*, Vol. 72, 1987, pp. 277–298.

[9] Weiss, J., Maruszewski, J. P., and Smith, W. A., "Implicit Solution of Preconditioned Navier-Stokes Equations Using Algebraic Multigrid," *AIAA Journal*, Vol. 37, No. 1, Jan. 1999, pp. 29–

36.

[10] Bigarella, E. D. V., *Advanced Turbulence Modelling for Complex Aerospace Applications*, Ph.D. thesis, Instituto Tecnológico de Aeronáutica, São José dos Campos, SP, Brazil, Oct. 2007.

[11] Hellsten, A., *New Two-Equation Turbulence Model for Aerodynamics Applications*, Ph.D. thesis, Helsinki University of Technology, Laboratory of Aerodynamics, P.O.Box 4400, Finland, Jan. 2004.

[12] Barth, M., Calmels, B., and Aupoix, B., "Numerical Simulation and Modelling of High-Lift Aerodynamics in Ground Effect," *Proceedings of the 27th International Congress of Aeronautical Sciences – ICAS 2010*, Paper No. 393, Nice, France, Sept. 2010.

[13] Wilcox, D. C., *Turbulence Modeling for CFD*, DCW Industries, La Cañada, CA, 2nd ed., 1998.

[14] Batten, P., Leschziner, M. A., and Goldberg, U. C., "Average-State Jacobians and Implicit Methods for Compressible Viscous and Turbulent Flows," *Journal of Computational Physics*, Vol. 137, No. 1, Oct. 1997, pp. 38–78.

[15] Peroomian, O., Chakravarthy, S., Palaniswamy, S., and Goldberg, U., "Convergence Acceleration for Unified-Grid Formulation using Preconditioned Implicit Relaxation," *36th AIAA Aerospace Sciences Meeting and Exhibit*, AIAA Paper No. 98-0116, Reno, NV, Jan. 1998.

[16] Roe, P. L., "Approximate Riemann Solvers, Parameter Vectors, and Difference Schemes," *Journal of Computational Physics*, Vol. 43, No. 2, Oct. 1981, pp. 357–372.

[17] van Leer, B., "Towards the Ultimate Conservative Difference Scheme. V. A Second-Order Sequel to Godunov's Method," *Journal of Computational Physics*, Vol. 32, No. 1, July 1979, pp. 101–136.

[18] Barth, T. J. and Jespersen, D. C., "The Design and Application of Upwind Schemes on Unstructured Meshes," *27th AIAA Aerospace Sciences Meeting*, AIAA Paper No. 89-0366, Reno, NV, Jan. 1989.

[19] Holmes, D. G. and Connell, S. D., "Solution of the 2D Navier-Stokes Equations on Unstructured Adaptive Grids," *Adaptive Grids AIAA 9th Computational Fluid Dynamics Conference*, AIAA Paper No. 89-1932, June 1989.

[20] Chakravarthy, S., "A unified-grid finite volume formulation for computational fluid dynamics," *International Journal for Numerical Methods in Fluids*, Vol. 31, No. 1, 1999, pp. 309–323.

[21] Craft, T. J., Launder, B. E., and Suga, K., "Development and Application of a Cubic Eddy-Viscosity Model of Turbulence," *International Journal of Heat and Fluid Flow*, Vol. 17, No. 2, 1996, pp. 108–115.

[22] Wallin, S. and Johansson, A. V., "An Explicit Algebraic Reynolds Stress Model for Incompressible and Compressible Turbulent Flows," *Journal of Fluid Mechanics*, Vol. 403, Jan. 2000, pp. 89–132.

[23] Spalart, P. R., "Strategies for Turbulence Modelling and Simulation," *International Journal of Heat and Fluid Flow*, Vol. 21, 2000, pp. 252–263.

[24] Shur, M. L., Strelets, M. K., Travin, A. K., and Spalart, P. R., "Turbulence Modeling in Rotating and Curved Channels: Assessing the Spalart-Shur Correction," *AIAA Journal*, Vol. 38, No. 5, 2000, pp. 784–792.

[25] Spalart, P. R. and Allmaras, S. R., "A One-Equation Turbulence Model for Aerodynamic Flow," *La Recherche Aeropastiale*, Vol. 1, Jan.-Feb. 1994, pp. 5–21.

6 Contact Author Email Address

E.D.V. Bigarella, enda.bigarella@embraer.com.br

Copyright Statement